Search for narrow states in the inclusive γ-ray spectra resulting from antiproton annihilations at rest in liquid hydrogen and deuterium

N.A. Graf,* M. Fero,† M. Gee, M. Mandelkern, R. Ray,* D. Schultz,† J. Schultz, and T. Usher†
Department of Physics, University of California, Irvine, California 92717

T.A. Armstrong, J. Biard, R.A. Lewis, S.M. Playfer,‡ G.A. Smith, and M.J. Soulliere
Laboratory for Elementary Particle Science, Department of Physics, Pennsylvania State University, University Park, Pennsylvania 16802

B. Bassalleck, D.M. Wolfe, and P. Denes
Department of Physics and Astronomy, University of New Mexico, Albuquerque, New Mexico 87131

G. Büche, L. Bürcker, H. Koch, and J. Schwertel
Kernforschungszentrum Karlsruhe, Institut für Kernphysik and Universität Karlsruhe, Institut für Experimentelle Kernphysik, D-7500 Karlsruhe 1, Federal Republic of Germany

A. Angelopoulos, A. Apostolakis, H. Rozaki, and L. Sakelliou
Nuclear Physics Laboratory, University of Athens, Athens 144, Greece
(Received 14 March 1991)

The energy spectrum of γ rays produced in proton-antiproton annihilation at rest in hydrogen and deuterium has been measured with good energy resolution and high statistics. The data were taken using the PS183 magnetic pair spectrometer at CERN's Low Energy Antiproton Ring. A detailed search of the γ spectrum yielded no evidence of γ transitions to narrow states with widths consistent with the spectrometer resolution. In hydrogen, upper limits (95% C.L.) are obtained for the yield of narrow states of $(2\text{–}5)\times10^{-4}$ for states below 1700 MeV/c^2, and $(5\text{–}10)\times10^{-4}$ for states between 1700 and 1800 MeV/c^2. In deuterium, the corresponding upper limits are $(1\text{–}7)\times10^{-3}$ for masses between 700 and 1730 MeV/c^2, and $(1\text{–}2)\times10^{-3}$ for masses between 1750 and 1835 MeV/c^2. These results contradict reports of the observation of narrow lines made by previous experiments.

I. INTRODUCTION

This paper presents the results of a search for narrow states produced in antiproton-proton and antiproton-deuteron annihilations at rest in liquid hydrogen and deuterium targets. Evidence for such states, produced in the reaction $\bar{p}p \rightarrow \gamma X$, would appear in the inclusive γ-ray energy spectrum as narrow peaks superimposed on a large but smooth background resulting from π^0 decays. A search of this type was conducted in CERN experiment PS183, on which this report is based.

Depending on the theoretical model employed, the observation of such narrow lines could be interpreted as either evidence for radiative transitions to narrow "quasinuclear bound states" of a nucleon-antinucleon pair [1], or as evidence for the existence of four-quark bound states, or "baryonium" [2]. Calculations based on nucleon-antinucleon potentials [3] as well as on "bag models" [4] predict rich spectra of states in both the isospin 0 and 1 $N\bar{N}$ systems.

Evidence for the existence of such states has been reported, based on experimental observations of narrow lines in the inclusive γ-ray spectrum from $\bar{p}p$ annihilations at rest [5]. Although the number of reported structures is rather large, and some correspondences exist among the lines reported in different experiments, the statistical significance of most of the lines is low. The low yield of these narrow lines places them at the limit of the experimental sensitivities.

Central to the success of the PS183 experiment was the unique antiproton storage and deceleration facility available at CERN's Low Energy Antiproton Ring (LEAR). The high intensity and duty factor of the LEAR antiproton beam meant that high-statistics experiments could be done in a fairly short time. The well-defined momentum of the pencil-thin beam made the analysis of in-flight events, and the determination of the stopping point, much easier than in the case of conventional secondary antiproton beams. The problems due to contamination of the beam from other particles, normally associated with traditional secondary beams, are entirely eliminated. The very low energies attainable for the extracted

beams also means that energy degraders are unnecessary, resulting in much narrower stopping distributions.

The PS183 magnetic pair spectrometer with its intrinsically good resolution, coupled with the clean, high-rate, low-momentum antiproton beam from the LEAR facility at CERN, formed an ideal experimental environment to perform a high-statistics, high-resolution experimental measurement of the inclusive γ-ray spectrum and resolve some of the experimental uncertainties.

The hydrogen data discussed in this paper were collected during two separate runs. The first run occurred with a liquid-hydrogen target, incident beam momenta of 450 and 330 MeV/c and a field setting of 3.5 kG. The second data collection run took place with beam momenta of 430 and 350 MeV/c at a field setting of 7.5 kG. The deuterium data were accumulated during a single run, at 7.5 kG with incident antiprotons at 350 MeV/c. Results of an analysis of the first-run hydrogen gamma ray data can be found in Ref. [6] and further details of the analysis can be found in Refs. [8]–[10]. Further details of the analysis of both the second-run hydrogen data and the deuterium data are found in Ref. [7]. Analyses of the charged-meson spectra collected by PS183 can be found in Ref. [11].

This paper is organized as follows: Section II describes the experimental setup and the components of the detector. The trigger logic and data-acquisition system are presented in Sec. III. A Monte Carlo analysis used to simulate the γ-ray spectrum from annihilations and the detector response function are described in Sec. IV. Section V discusses the event-reconstruction procedures and the methods used to calibrate the spectrometer. Sections VI and VII give the final spectra obtained and the statistical procedures used to search for narrow states; final results, consisting of limits on yields, are presented. Section VIII gives our conclusions.

II. THE EXPERIMENTAL SETUP

The experimental setup as it existed during the second hydrogen run is shown in Figs. 1 and 2. The PS183 detector consisted of scintillation counters (S, Halo, A1-A6, Q, V, D1, D2, E1, E2, P1-P5, T, N1-N4), multiwire proportional chambers (2 beam chambers, CWC, B, C1, C2, D1, D2, E1, E2) and planar drift chambers (N1,2, R1,2, P1,2). The counters were used in forming the trigger and also for time-of-flight calculations for particle identification. The wire chambers were used to determine the trajectories of charged particles in order to determine the annihilation vertex and also to measure the momentum of those particles entering the spectrometer.

A. Target instrumentation

The front-end of the detector consisted of the target assembly and the detectors used to determine the incoming antiproton beam and the annihilation vertices. Although very well focused ($\sigma_{\text{beam}} \simeq 0.3$ cm), the beam needed to be fine-tuned to correct for changes in the polarity of the magnetic field setting of the spectrometer. Therefore, two small multiwire proportional chambers were placed between the beam snout (0.01 cm beryllium membrane) and the target. These chambers were identical in construction and each contained a Y and Z plane of wires (20 μm gold-plated tungsten) with 1-mm wire spacing. The cathode planes consisted of 0.0025 cm aluminized Mylar sheets. A 69% argon, 29.5% isobutane, and 1.5% Freon gas mixture was bubbled through isopropyl alcohol at 8° and sent to the beam chamber and the cylindrical multiwire proportional chamber surrounding the target. The alcohol was needed to cure the chambers of aging effects and also to limit the space charge in the high-rate chambers. A total of 32 wires were instrumented in each plane and the respective planes of the two chambers were separated by 20 cm, allowing the direction of the incoming antiproton to be reconstructed. The beam then passed through a small (2.0×2.5 cm^2), 0.08-cm-thick Bicron 400 plastic scintillation counter (S2). A pulse in the

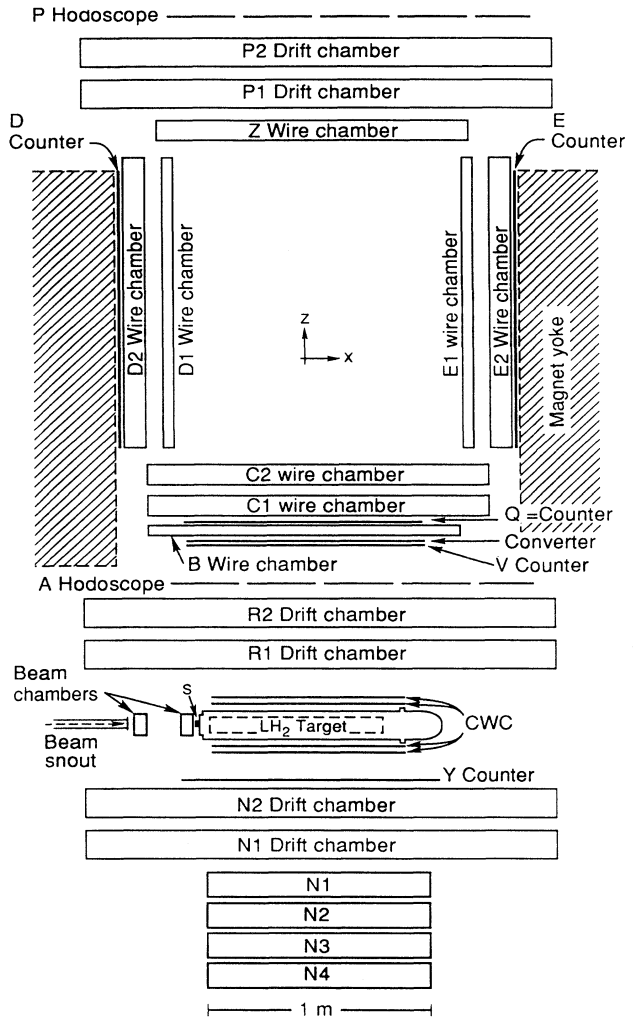

FIG. 1. Plan view of the PS183 experiment. Antiprotons entered the detector from the left.

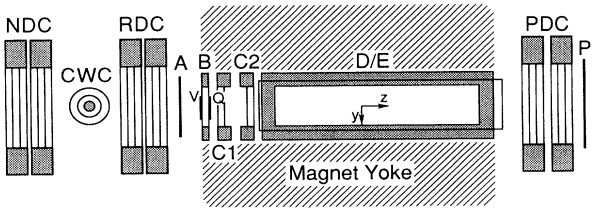

FIG. 2. An elevation view of the PS183 experiment, looking upstream.

S2 counter signaled the entrance of an antiproton into the target and was used to start the trigger logic as well as all timing circuits for the data-acquisition system. A halo counter was installed around the S2 counter to ensure that events with antiprotons missing the S2 counter but still entering the target could be vetoed.

The target vessel was a 0.0125-cm-thick Mylar cylinder 7 cm in diameter and roughly 70 cm in length. This was insulated by vacuum and centered by Rohacell spacers in an outer cylinder (84.0 cm in length and 12.5 cm in diameter) of 0.25-cm-thick Dallite. It was mounted in such a fashion that it could be moved along the beam axis to ensure that the antiprotons would range and come to rest at the centerline of the spectrometer. Because of the very high momentum resolution of the LEAR beam ($\delta p/p \simeq 10^{-3}$), the stopping position was very well defined and could be accurately calculated. The beam ranged ~ 56 cm in the target for an incident antiproton momentum of 430 MeV/c and ~ 24 cm for 350 MeV/c antiprotons.

During the second hydrogen run the target assembly was surrounded by a cylindrical multiwire proportional chamber (CWC) to measure the charged multiplicity of the annihilations and assist in the annihilation vertex reconstruction. The CWC consisted of two cylindrical layers of sense wires with 3-mm-wire spacing. The inner layer had a radius of 7.8 cm and contained 160 wires (2.25° separation), whereas the outer layer contained 224 wires at a radius of 10.9 cm (1.60°); in both cases the wire spacing was approximately 3 mm. Each cathode consisted of a thin layer of graphite applied to the four concentric Dallite cylinders separating the G-10 end caps. The cathode-anode separation was 0.8 cm. The active area of the chamber was 70 cm long and the CWC was centered on the stopping point of the beam.

Flanking the target assembly on both sides were two arrays of planar drift chambers, R1,2 between the target and spectrometer, and N1,2 opposite. Each of the drift chambers consisted of identical pairs of x, u, and v planes containing 39 drift cells oriented at 0°,+30°, and −30° to the vertical. The chambers were operated with a 75%–25% mix of argon-isobutane at NTP. The active area of each of the chambers was 130 cm by 53 cm. All charged annihilation products entering the spectrometer thus passed through R1,2. Each drift chamber provided six measurements of a charged particle's trajectory, enabling a full reconstruction of the track. These tracks, combined with the beam chamber track of the incoming antiproton, enabled an accurate reconstruction of the annihilation vertex. In order to be able to calculate annihilation vertex positions on line, the drift chambers N1,2 were modified by the addition of another set of sense wires placed next to the existing sense wires. This double-wiring removed the left-right ambiguity inherent in drift chamber hits and enabled a fast on-line reconstruction of the particle's trajectory, thus allowing the annihilation vertex to be constantly monitored.

B. The spectrometer

The spectrometer itself was centered on the 120 ton MEP-21-2 electromagnet. The aperture of the magnet was $154 \times 50 \times 176$ cm^3, with the actual pole-face dimensions of 112 cm × 151 cm in X and Z, respectively. The magnetic field was mapped both within and around the magnet at several field settings (3.5, 7.5, and 15 kG) and a parametrization of the field to better than 0.5% was obtained. The central value of the field during the first hydrogen run was 3.5 kG; that of the second hydrogen and the deuterium run was 7.5 kG. The polarity of the field was reversed during the running to obtain roughly equal amounts of data at the two settings. The magnitude of the field was constantly monitored with a Hall probe mounted within the magnet aperture and maintained to within ±0.2%.

Shadowing the spectrometer was the A-counter hodoscope. This consisted of six identical NE102A double-ended plastic scintillators with dimensions $21.7 \times 40.0 \times 0.5$ cm^3. Located at the entrance of the spectrometer was a pair of identical scintillation counters (Q and V) sandwiching the B chamber and a thin lead foil. The arrangement of the counters allowed differentiation of a charged particle and γ ray. The double-ended counters were made of $80.0 \times 14.0 \times 0.5$ cm^3 pieces of NE102A plastic. The entrance of a charged particle into the spectrometer was signaled by a pulse in the V counter. The 0.06 cm ($\simeq 10\%$ of a radiation length) thick lead foil was used to convert incident γ rays into e^+e^- pairs. The 80.0×14.0 cm^2 foil located 71 cm from the target center subtended 1.53% of 4π steradians and defined the geometric acceptance for the γ rays produced in the annihilations. A pulse in the Q counter without a concomitant pulse in the V counter signaled the creation of an e^+e^- pair. Delayed hits in the V counter were tolerated for the R-track topology, since the returning electron sometimes hits the V counter.

The aperture of the magnet was instrumented with seven multiwire proportional chambers. The sense wire planes consisted of 20-μm gold-plated tungsten wires strung at a tension of 50 g and positioned 3 mm apart. The cathode planes consisted of 50-μm beryllium-copper wires tensioned to 200 g and positioned at 1 mm intervals. The anode-cathode separation was 0.8 cm and the chambers were operated with a 70% argon, 30% isobutane, 0.15% Freon gas mixture bubbled through isopropyl alcohol at 12°. Vertical (X plane), horizontal (Y plane),

and oblique (U plane, 45° for limited stereo resolution) wires were instrumented. The X planes contained 416 sense wires covering an active area of 124.5×26.7 cm^2. The B chamber consisted of only an X plane, the D1 and E1 chambers contained X and Y planes, and the remaining chambers were fully instrumented.

The side counters (D and E) were each composed of two nearly identical NE110 plastic scintillators [$127.0 \times 13.1 \times 0.5$ cm^3 for the D1 (E1) and $127.0 \times 15.0 \times 0.5$ cm^3 for the D2 (E2)]. Because of spatial restrictions, these counters were only read out at one end. To the rear of the magnet was another pair of drift-chamber triplets P1,2 identical to R1,2, followed by the P counter hodoscope. The five double-ended P counters consisted of $32.0 \times 60.0 \times 0.5$ cm^3 pieces of NE102A plastic scintillator. Additionally, a bank of four identical NE110 plastic neutron counters ($100 \times 20 \times 10$ cm^3) was placed on the far side of the drift chambers N1,2. These counters were double ended and calibrated with a ^{60}Co source. Shadowing this assembly was the T counter, providing time-of-flight information as well as fast charged-particle vetoing.

III. THE DATA-ACQUISITION SYSTEM

During the data runs, the γ-ray data-acquisition system was configured to accept four distinct types of γ ray events. Typical electron and positron tracks for these event topologies are shown in Fig. 3. Depending upon the momentum of the individual particle, three distinct topologies are allowed: the particle may be reflected by the magnetic field of the spectrometer giving rise to an "R" (for returning) track; it may be deflected by approximately 90° and be stopped in the yoke of the magnet leading to a "T" (for trapped) track; or, if the momentum is sufficiently high, the particle may suffer only a small deflection from its original path and pass completely through the spectrometer, resulting in a "P" (for penetrating) track. Differing combinations of initial γ-ray energy and the energy sharing between the electron-positron pair lead to the four topologies shown in Fig. 3, namely RR, RT, TT, and PT. The low acceptance for other possible combinations led to the decision not to trigger on such events. Returning tracks were distinguished from incident charged particles by comparing the timing of the Q counter hit and the hit in the A hodoscope using a sub-nanosecond time discriminator system [12]. If the hit in the A hodoscope was later than that of the Q counter it was labeled a "late A" hit and was considered a returning track.

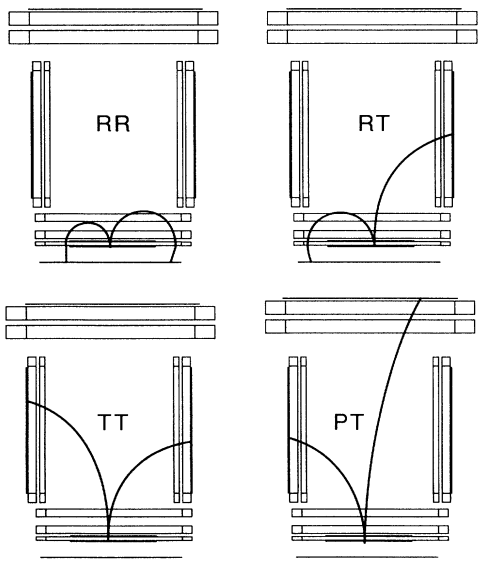

FIG. 3. Shown are the four allowed γ ray topologies in the hydrogen (second run) and deuterium data set; (a) returning-returning (RR), (b) returning-trapped (RT), (c) trapped-trapped (TT), (d) penetrating-trapped (PT).

A. The experiment trigger

In order to accommodate the high rates experienced at the LEAR facility (on the order of 10^5 incident antiprotons per second), it was necessary to implement a multi-level trigger. The trigger was formed in two distinct stages; a hardware pretrigger based on conventional Nuclear Instrument Module (NIM) standard logic and a computer-controlled second stage employing CAMAC programmable logic units (PLU's) and was based on scintillator hit patterns.

B. The NIM pretrigger logic

The experiment pretrigger was designed to identify an incoming antiproton, generate necessary coincidence gates to identify further activity in the spectrometer and strobe the next stages of the trigger. This pretrigger was based on fast NIM logic using the signals from the scintillation counters. A schematic logic diagram for this pretrigger is shown in Fig. 4. The pretrigger was formed in a series of stages, each initiating an appropriate hold-

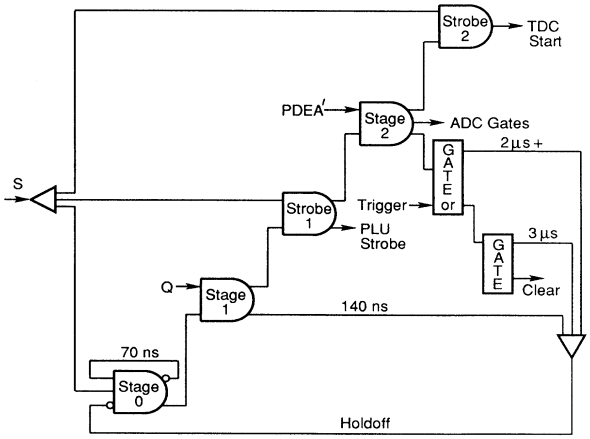

FIG. 4. Schematic of the NIM-based experiment pretrigger logic circuit.

off to allow the results necessary for the next stage to be analyzed. To reduce the front-end electronic dead time, analog-to-digital converters (ADC's) and time-to-digital converters (TDC's) were not strobed until the pretrigger was formed. The entrance of an antiproton into the liquid-hydrogen target was signaled by a pulse in the S2 counter. The arrival of this signal was used to start all clocks used in the experiment and constituted a stage 0 trigger. A coincidence between this signal and a pulse from the Q counter (located at the entrance to the spectrometer) indicated that an annihilation had taken place and that at least one of the decay products had entered the spectrometer. This stage 1 pretrigger was used to strobe the PLU's, ensuring that the delayed scintillator signals arrived in coincidence with the PLU gates. Further activity within the spectrometer was signaled by pulses from any of the remaining counters: a "late A" (A′) hit indicates a returning track, a D or E counter hit signals a trapped track, and a hit in the P hodoscope indicates that a particle has exited through the back of the spectrometer. The final stage of the pretrigger was formed by a coincidence of any combination of these scintillator hits (labeled PDEA′ in the figure) and the stage 1 signal. At this point scintillator ADC gates are formed. The stage 1 output was clocked by a delayed S2 pulse and was used to start the scintillator TDC clocks. The system was held off until a trigger decision from the PLU's was made. If the next stage did not issue a trigger, a fast clear was sent to the ADC and TDC modules.

C. The CAMAC trigger

The pretrigger asserted only that an antiproton had entered the target and annihilation products had entered and exited the spectrometer. Because of the large number of possible event topologies and the desire to be able to modify the experiment trigger on-line, the next stage of the experiment trigger was formed using relatively fast memory look-up modules to form the final trigger. The final trigger was made in six CAMAC-based LeCroy 4508 PLU's. The first four PLU's encoded and compacted the scintillator hits. These inputs were latched and later used to form a scintillator hit code, which indicated exactly which scintillators had fired. The outputs were directed to the TPLU which formed the final trigger based on the topology of scintillator hits. The allowable scintillator hit patterns were determined beforehand and programmed into the memory of the PLU. If a match was made, the trigger, along with the trigger type (charged particle trigger, γ-ray trigger, etc.) was sent to the CPLU which decided whether to accept the trigger. This final stage allowed certain trigger types, such as charged particle triggers, to be attenuated and could be easily modified if a different mix of triggers was desired. The final CPLU trigger was sent to the NIM logic, which continued the trigger hold off, and to the data-acquisition system to initiate the event readout.

D. Event readout

Once triggered, the data-acquisition system had to obtain the event information from three major systems: the MWPC wire hits, the drift-chamber wire hits and TDC information, and the scintillation counter TDC and ADC data. The raw data was then buffered into event data packets and written to magnetic tape. The principal data streams in the data acquisition system are shown in Fig. 5.

The data collection rate was optimized by utilizing four computers in the data acquisition system. Each of the computers used was uniquely suited to its task: the event readout and buffering was accomplished by high-speed low-level microprocessors, the data logging and on-line numerical analysis by an efficient high-speed PDP-11 computer, and on-line diagnostics and overall control of the experiment was accomplished by an intelligent and user-friendly (but relatively slow) HP9826 desk top computer. By distributing the data acquisition tasks in such a way as to take advantage of the strengths of the individual processors, the data acquisition rate was practically limited only by the rate at which data could be written to magnetic tape.

Central to the data-acquisition system were two high-speed microprocessors resident in a CAMAC environment. The LeCroy 4805 (BG*) CAMAC Booster (CAB) was used to read in the raw data from the MWPC and drift chamber data buffers and the scintillator ADC's and TDC's. The MWPC and drift chamber data were transferred directly from the two Model 4299 data buffers in a

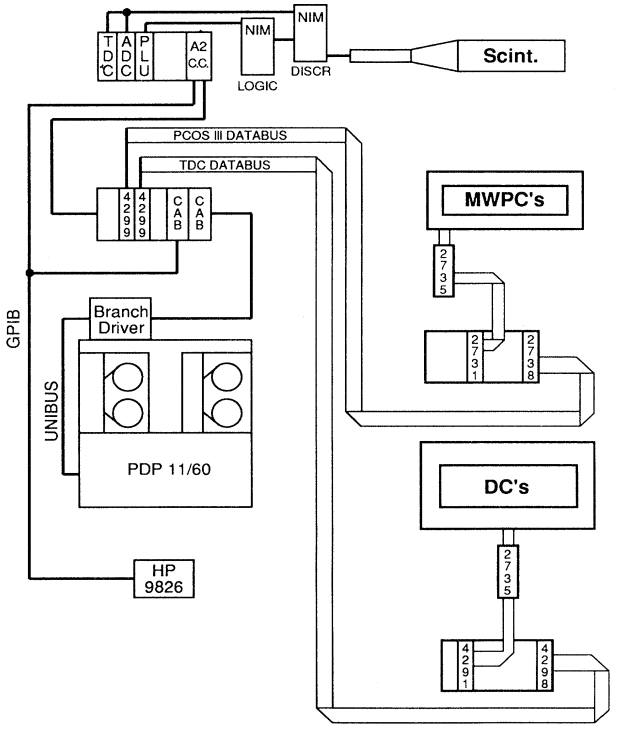

FIG. 5. The principal data streams for the PS183 spectrometer.

compact, formatted form. In order to keep the size of the event data packets to a minimum, the scintillator TDC and ADC was read only for those counters which actually fired. The scintillator hit code was available from the latched inputs to the PLU's in the trigger logic. The full event data packet was then transferred to another CAB (LeCroy Model 4804 (CG*) which served to buffer the events according to their topology type. A clear signal was sent to the NIM pretrigger logic system, which cleared the ADC and TDC modules and initiated a $3\mu s$ holdoff, allowing the TDC modules to clock down. After this holdoff had expired the system was again "live" for another event.

Full data buffers were then sent to a DEC PDP 11/60 computer which wrote the data to magnetic tape. Additionally, the PDP served to provide on-line diagnostic information. Raw data such as wire hit profiles in the various chambers, as well as scintillation counter ADC and TDC spectra were histogrammed. Information from the beam chamber and N1,2 (which, as indicated above, was double wired to eliminate the left-right ambiguity of drift chamber hits and speed up the track-reconstruction calculation) was also used to reconstruct annihilation vertices, assuring that the antiprotons were stopping in the target.

The data acquisition system as a whole was controlled by a Hewlett-Packard 9826 minicomputer. During the data-taking periods, the HP9826 was used to start and stop runs, and provided on-line graphic snapshots of the detector performance. Trigger configurations could also be quickly changed between spills. The goal of the data-acquisition system was to write as many high-quality data events to tape as possible. Typically, the system wrote about 300 events/sec to tape. During the second run data run, over 600 1600 bpi tapes were written.

IV. MONTE CARLO SIMULATION

Since the goal of experiment PS183 was to search for monochromatic gamma rays with yields on the order of 10^{-4} *per* $\bar{p}p$ annihilation, it was essential that the background spectrum and the spectrometer characteristics be well understood. Fundamental to the search for narrow lines in the spectra was a full understanding of the energy resolution and acceptance of the spectrometer.

The predominant source of background γ rays in this experiment was the decay of neutral pions produced in the annihilation of antiprotons at rest. On average, 1.8 π^0's are produced per $\bar{p}p$ annihilation at rest. These π^0's then decay into pairs of photons. In order to simulate this γ-ray background, published data on exclusive final state production from $\bar{p}p$ annihilations at rest were used to generate an inclusive γ-ray spectrum (see Fig. 6). Since the γ rays resulting from the decays of neutral pions are by far the predominant source of background, only these channels were used in simulating the spectra. Differences between the simulated and experimental spectra would then reveal alternate sources of γ rays, which would be of interest. Table I contains a list of the annihilation channels, along with the intermediate resonances and branching ratios, used in the Monte Carlo simulation of the inclusive γ-ray spectrum resulting from $\bar{p}p$ annihilations at rest. A comprehensive compilation of published annihilation channels can be found in Ref. [13].

Antiproton annihilations at rest in deuterium were first studied by Chinowsky and Kojoian [14]; because of the paucity of data on specific annihilation channels, however, a separate Monte Carlo γ spectrum resulting from antiproton annihilations in deuterium was not generated. The spectrum was fit to the following functional form, similar to that found in Ref. [15]:

$$F(E_\gamma) = N_\gamma \left[(E_0 - E_\gamma)^{\alpha_1} e^{\beta_1} + (E_0 - E_\gamma)^{\alpha_2} e^{\beta_2} + \beta_3 e^{\alpha_3 E_\gamma} \right] ,$$

where

TABLE I. $\bar{p}p$ branching ratios used in the γ Monte Carlo simulation. Branching ratios used for the first-run hydrogen analysis are slightly different [8].

Channel	Final state	Intermediate state	Yield
1	$\pi^0 2\gamma$	$\pi^0\eta^0$	0.32
2	$2\pi^0\gamma$	$\pi^0\omega^0$	0.25
3	$4\pi^0$	$\pi^0\eta^0$	0.26
4	$3\pi^0$		1.70
5	$4\pi^0$		0.16
6	$5\pi^0$		1.07
7	$\pi^+\pi^-$		0.32
8	$\pi^+\pi^-\pi^0$		0.84
9	$\pi^+\pi^-\pi^0$	$\pi^0 f^0$	0.24
10	$\pi^+\pi^-\pi^0$	$\pi^+\rho^-$	3.87
11	$\pi^+\pi^-\pi^0$	$\pi^0\rho^0$	1.94
12	$\pi^+\pi^-2\pi^0$		7.01
13	$\pi^+\pi^-2\pi^0$	$\pi^0\omega^0$	2.10
14	$\pi^+\pi^-2\pi^0$	$\pi^0\eta^0$	0.19
15	$\pi^+\pi^-3\pi^0$		23.30
16	$\pi^+\pi^-4\pi^0$		2.80
17	$2\pi^+2\pi^-$		2.38
18	$2\pi^+2\pi^-$	$\pi^+ A_2^-$	2.00
19	$2\pi^+2\pi:-$	$\rho^0 f^0$	0.90
20	$2\pi^+2\pi^-$	$\pi^+\pi^-\rho^0$	1.50
21	$2\pi^+2\pi^-$	$\rho^0\rho^0$	0.12
22	$2\pi^+2\pi^-\pi^0$	$\pi^+\pi^-\eta^0$	0.35
23	$2\pi^+2\pi^-\pi^0$	$\pi^+\pi^-\pi^0\rho^0$	7.30
24	$2\pi^+2\pi^-\pi^0$	$2\pi^+\pi^-\rho^0$	6.40
25	$2\pi^+2\pi^-\pi^0$	$\omega^0 f^0$	1.66
26	$2\pi^+2\pi^-\pi^0$	$\omega^0\rho^0$	2.02
27	$2\pi^+2\pi^-\pi^0$	$\pi^+\pi^-\omega^0$	2.23
28	$2\pi^+2\pi^-2\pi^0$		16.60
29	$2\pi^+2\pi^-3\pi^0$		4.20
30	$3\pi^+3\pi^-$		1.90
31	$3\pi^+3\pi^-\pi^0$	$2\pi^+2\pi^-\eta^0$	0.72
32	$3\pi^+3\pi^-\pi^0$	$2\pi^+2\pi^-\omega^0$	1.30
33	$3\pi^+3\pi^-2\pi^0$		0.30
Total			98.25

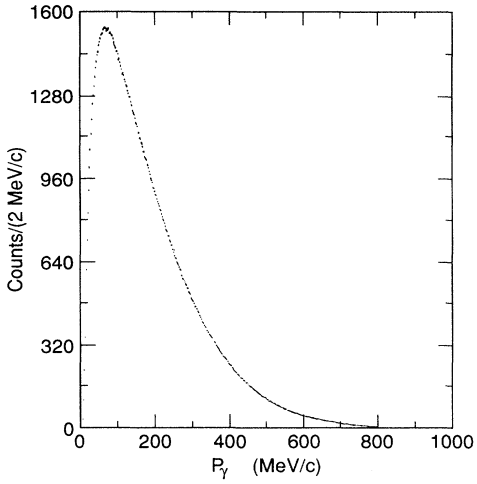

FIG. 6. The inclusive Monte Carlo γ spectrum.

$$E_0 = 938.28 \text{ MeV} , \quad N_\gamma = 3.84 ,$$
$$\alpha_1 = 4.4481 , \quad \beta_1 = -34.8344 ,$$
$$\alpha_2 = 1.5471 , \quad \beta_2 = -17.9968 ,$$
$$\alpha_3 = -0.035\,17 \text{ MeV}^{-1} , \quad \beta_3 = -0.015\,32 .$$

In the fit, E_0 and N_γ were fixed parameters and a χ^2 degree of freedom of 1.1 was obtained. This expression is normalized to give N_γ photons per annihilation. There are many estimates for N_γ, including one direct experimental determination which gave $N_\gamma = 3.78 \pm 0.08$ [16]. Using the average number of π^0's produced at rest in $\bar{p}p$ annihilations from Ref. [17] ($\langle n_{\pi^0} \rangle = 1.96 \pm 0.23$), one obtains a value of $N_\gamma = 3.92$. The value used in the fit is an average of the number of γ rays produced by the channels used in the Monte Carlo simulation. An indirect measurement by Kalogeropoulos *et al.* [18] of the average number of photons produced in the annihilations of antiprotons at rest in deuterium yielded 3.77 ± 0.08 in apparent disagreement with the number expected from isospin invariance. However, an experiment by Amsler *et al.* [19] measured a mean γ-ray multiplicity of 2.6 ± 0.3 for antiproton annihilations at rest in liquid deuterium, consistent with the number expected (3.04). This Monte Carlo–generated sample was then used to simulate the experimental spectra.

A. Simulating the detector

The PS183 detector was modeled using the GEANT 3.10 detector simulation code developed at CERN. To determine the response of the PS183 detector to γ rays produced in antiproton annihilations, monochromatic γ rays were generated in the target and randomly populated the lead converter. At the end of each event in which the photon converted, the scintillator hit pattern was sent to a triggering subroutine which used the same criteria for a valid γ event as the experiment hardware trigger logic. If the event passed the trigger requirement, the momenta of the electron and positron tracks were calculated using the analysis routines and histogrammed. This procedure was then repeated for various input energies and final-state topologies, since the resolution of the spectrometer depended not only on the momentum but also on the topology type. It was therefore necessary to fit the response functions for each topology as well as each input momentum. The response functions were then parametrized by a function of the form

$$R(E,E') = h(E') \exp\left(-\frac{[E-\mu(E')]^2}{2\{\sigma(E') - \lambda(E')[E-\mu(E')]\}^2}\right)$$

where λ=0 for $E > \mu(E')$. This functional parametrization accounts for the low-energy tail due to bremsstrahlung and Landau energy loss with the skewness parameter λ. The Gaussian nature of the momentum reconstruction routine is included by setting λ to zero above the peak of the spectrum. More sophisticated functions could have been used, but this particular form was chosen for its relatively small number of parameters and its ability to fit the spectra over the whole range of momenta and topologies ($\chi^2/N_{\rm DF}$ were typically less than 1.2). Figure 7 shows an example of the fit to a TT response function to a 250 MeV input γ ray line. The four parameters h, μ, λ, and σ were then plotted as functions of the input γ-ray energy and fit with low-order polynomials. This provided a smooth interpolation of the parameters for those momenta not explicitly input to the Monte Carlo program. The most probable energy lost $[E - \mu(E)]$ was roughly constant at 3 MeV and the skewness parameter λ was approximately 0.3 over the entire range of energies and topologies. Figure 8 shows the full width at half maximum (FWHM) resolution for the various detector event topologies. The resolution claimed by other recent experiments is shown for comparison. Figure 9 shows the

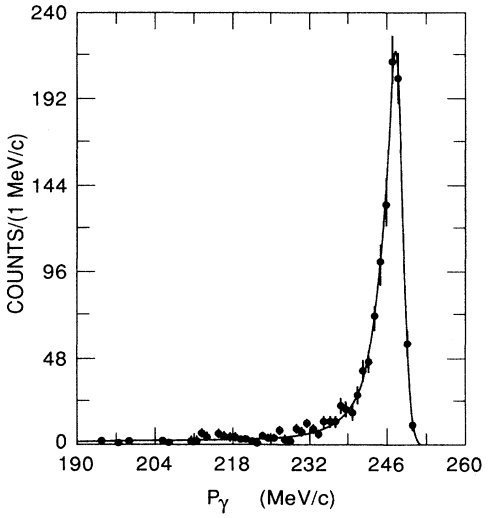

FIG. 7. The response function of the PS183 spectrometer to an input γ ray with incident energy of 250 MeV.

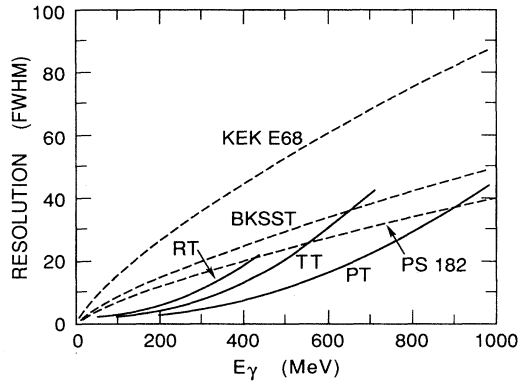

FIG. 8. Shown are the Monte Carlo detector resolutions (FWHM) for the *RT*, *TT*, and *PT* event topologies for 3.5 kG field strengths. The BKSST [15], PS182 [22], and KEK-E68 [21] resolutions are shown for comparison.

Gaussian resolution (σ) for the various topologies and field strengths of the spectrometer at the 7.5-kG field setting. In addition to providing the resolution of the spectrometer, the response functions were also used to generate Monte Carlo simulations of the various spectra.

B. Simulating the experimental spectra

Simulating the spectra involved convoluting the intrinsic γ-ray spectrum $G(E)$ with the response functions of the detector $R(E, E')$. The experimental spectrum $S(E)$ was then calculated via

$$S(E) = \int dE' \frac{h(E')}{H} G(E') \times \exp\left(-\frac{[E-\mu(E')]^2}{2\{\sigma(E')-\lambda(E')[E-\mu(E')]\}^2}\right) .$$

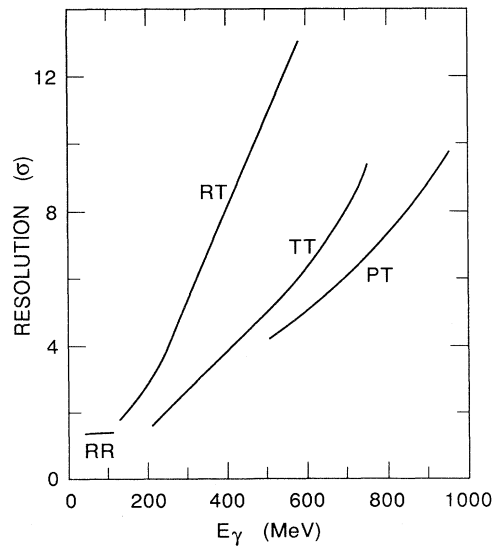

FIG. 9. Shown are the Monte Carlo detector resolutions (σ) for the *RR*, *RT*, *TT*, and *PT* event topologies for 7.5 kG field strengths.

V. EVENT RECONSTRUCTION

Associated with the data for each event written to tape by the data acquisition system was an event code based on the pattern of scintillation counters which were hit. The first requirement that the analysis program made on the data was that the pattern and number of hits in the wire chambers agree with the topology type determined by the pattern of hits in the scintillators. If the raw data did not pass the multiplicity filter, the hits were "reclustered." One-wire gaps between hit clusters were filled in the B, C1, and C2 chambers since the front chambers must properly discriminate between multiple closely spaced tracks, whereas the D and E chambers were allowed gaps of up to three wires, since only one track would ever cross any one side chamber, but often at a rather oblique angle. A new centroid and width for the cluster was calculated; if the event failed the multiplicity filter after reclusterization of the MWPC hits, it was discarded. Most of these discarded events were either real γ events accompanied by a charged pion or the result of electronic noise which caused too many wires to fire in a chamber. Because of the looseness of the hardware late-A trigger requirement in identifying returning tracks, the *RR* and *RT* sample suffered the greatest reduction at this stage: roughly 90% of the *RR* γ-triggered events were rejected.

A. Momentum reconstruction

Having now a sample of plausible e^+e^- events, the next step was to determine the momentum of each of the charged particles and thereby reconstruct the momentum of the incident γ ray. Two different algorithms were used to calculate momenta. For R and T tracks a three-point circle fit to the MWPC hits plus a momentum- and position-dependent correction factor to account for the inhomogeneities in the magnetic field was used. For P tracks a cubic spline fit reconstruction of the path of the particle, and thus a direct determination of the momentum, was used.

A scintillator timing cut was then applied to the data, requiring that the particle time of flight be consistent with an electron of the reconstructed momentum. A loose opening angle cut was then applied, to ensure that the electron and positron originated from the same point. The summed momenta of the two tracks were then histogrammed. To ensure that the momentum reconstruction was correct, several calibration lines were checked.

B. Momentum calibration

Several processes producing monochromatic particles in the final state are present in the annihilation of an-

tiprotons at rest in the liquid-hydrogen target. An analysis of the peaks produced by these particles allowed the spectrometer to be calibrated, checking the momentum reconstruction as well as the spectrometer resolution.

In the γ-ray spectra the only significant monoenergetic γ ray is the so-called Panofsky γ at 129 MeV, resulting from the reaction $\pi^-_{\text{stop}} p \rightarrow n\gamma$. This line was seen in the raw 3.5-kG RT and TT spectra and could be enhanced by requiring a Q counter hit 0.9 ns after the prompt signal. This signal enhancement is due to the delay associated with the negative pion ranging out in the target. A fit to this late Q spectrum with a Gaussian plus a smooth polynomial resulted in a peak centered at 125.5 MeV with a width of 3 MeV FWHM (Fig. 10). The energy loss, as well as the peak width were well in agreement with the Monte Carlo calculation. Unfortunately, during the second run at 7.5 kG, this calibration line fell into an acceptance gap between the RR and RT spectra. (It was seen, however, during a short calibration run at 3.5 kG.)

The monochromatic lines resulting from $p\bar{p} \rightarrow \pi^+\pi^-, K^+K^-$, in the charged particle spectra provided additional calibration lines at higher momenta. The lines are found in the charged-meson P track topologies at 3.5 kG, and in the P and T topologies at 7.5 kG (Fig. 11). Again, the widths and positions are in agreement with the resolution and energy loss expected in the spectrometer.

The decay of positive kaons, $K^+ \rightarrow \mu^+\nu_\mu$, $\pi^+\pi^0$, which are produced in the initial annihilation and come to rest in the target provided another source of monochromatic particles. The muons and charged pions appear in the charged T and P track topologies, providing a calibration point at intermediate energies. A complete analysis of this data can be found in Ref. [20].

In addition to peaks in the spectra due to monochromatic particles, kinematic edges from various neutral two-body processes will result in shoulders in the experimental spectra. For neutral two-body reactions $p\bar{p} \rightarrow \pi^0 X \rightarrow \gamma\gamma X$, the "box-end" energies of the γ energy distribution seen in the inclusive γ-ray spectrum will be

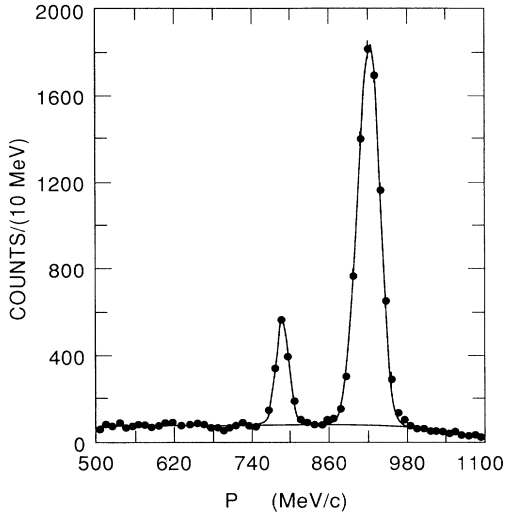

FIG. 11. The momentum spectrum of charged two-body annihilations of the $\bar{p}p$ system, $\bar{p}p \rightarrow \pi^+\pi^-$, and $\bar{p}p \rightarrow K^+K^-$.

given by

$$E^{\gamma}_{\text{max/min}} = \tfrac{1}{2}E(1 \pm \beta) ,$$

where E is the total energy of the decaying particle (π^0 in this case), and β is its velocity. The edges of this uniform distribution will be smeared by the spectrometer resolution and the intrinsic widths of the decaying particles. One of the more prominent reactions of this sort is $p\bar{p} \rightarrow \pi^0\omega$. Figure 12 shows the Monte Carlo–generated intrinsic γ-ray spectrum resulting from the reaction $p\bar{p} \rightarrow \pi^0\omega$. The sharp falloff at $\sim$ 770 MeV is quite apparent. Figure 13(a) shows a fit to the high-energy end of the Monte Carlo–generated TT spectrum, excluding the process $p\bar{p} \rightarrow \pi^0\omega$. This fit is shown superimposed

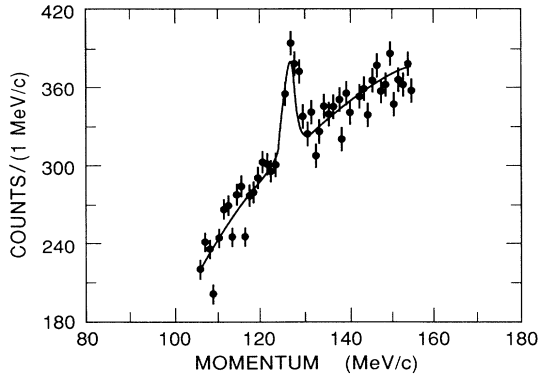

FIG. 10. The Panofsky gamma, as it appears in the late Q, combined RT plus TT γ spectrum, at 3.5 kG.

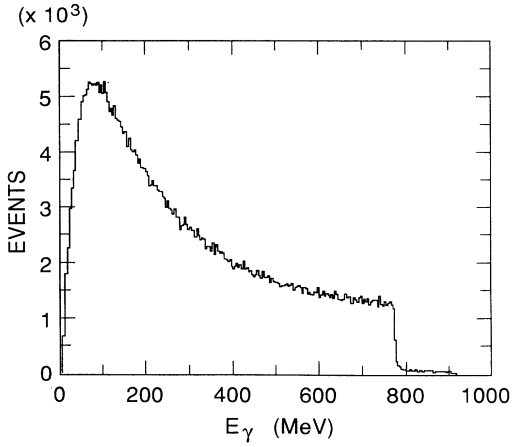

FIG. 12. The Monte Carlo–generated intrinsic γ-ray spectrum resulting from the reaction $p\bar{p} \rightarrow \pi^0\omega$.

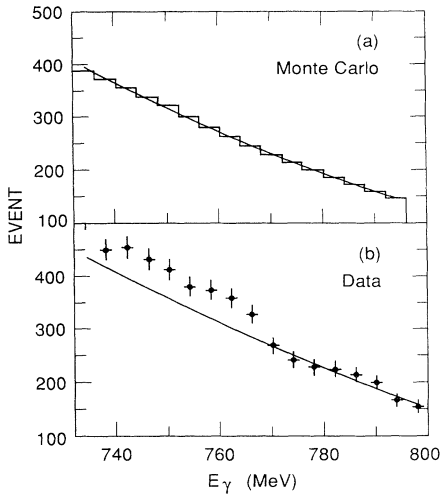

FIG. 13. A fit to the high energy end of the Monte Carlo–generated TT spectrum, excluding the process $p\bar{p} \rightarrow \pi^0\omega$, is shown in (a). This fit is shown superimposed on the actual TT spectrum in (b).

on the actual TT spectrum in Fig. 13(b). The break in the spectrum occurs at 768 MeV and provides us with another calibration point for the high-energy gamma spectra. A calculation of the branching ratio for $\pi^0\omega$ gives $(0.76 \pm 0.11)\%$. This value for the branching ratio is close to the value of $(0.52 \pm 0.05)\%$ reported by Chiba *et al.* [21], but differs somewhat substantially from the measurement of Adiels *et al.* [22] of $(2.38 \pm 0.65)\%$.

C. Annihilation vertex

A determination of the annihilation vertex was necessary to ensure that the annihilations were occurring in the liquid-hydrogen target and taking place at rest. For events containing charged particles in the final state which passed through either R1,2 or N1,2, a vertex could be reconstructed using the drift chamber track(s) and the beam-chamber track of the incident antiproton. However, in order not to bias the data sample against channels which contained only neutral particles in the final state, no explicit vertex cut was used in the analysis. Careful monitoring of the on-line vertex and a reconstruction of the vertices of events with charged particle tracks in the drift chambers ensured that the vast majority of the annihilations had indeed occurred within the target.

Even without an explicit determination of the annihilation vertex, those annihilations that took place at rest could be selected. The time required for the antiprotons to range in the target and come to rest is constant. Therefore, events which occur significantly earlier than normal are expected to have resulted from in-flight interactions (see Fig. 14). A plot of the predicted Q-counter time versus the projection onto the X axis of the target of the reconstructed annihilation vertex is shown in Fig. 15. A cut on early Q times enabled one to distinguish between in-flight and at-rest annihilations, even for events with an all-neutral final state. Most of those events having a correct Q time and an upstream annihilation vertex proved to be pions and were removed at a later stage of the analysis. Figure 16 shows a plot of the difference in the predicted and measured Q-counter time for the three data sets of the second data run (430 MeV/c antiprotons incident on a liquid-hydrogen target, 350 MeV/c $\bar{p}$'s incident on a liquid-deuterium target and 350 MeV/c $\bar{p}$'s incident on a liquid-hydrogen target). The differences in the plots reflect the different incident beam momenta as well as the different target compositions. The range, and hence the time required to come to rest, of the 430 MeV/c $\bar{p}$'s was longer than that of the 350 MeV/c $\bar{p}$'s. The number of events with very early Q times in Fig. 16(a) is simply a reflection of this longer path length. The roughly 2:1 ratio of in-flight interactions in Figs. 16(b) and 16(c) is a reflection of the 2:1 ratio of the densities of liquid deuterium and liquid hydrogen and, hence, the greater number of in-flight interactions.

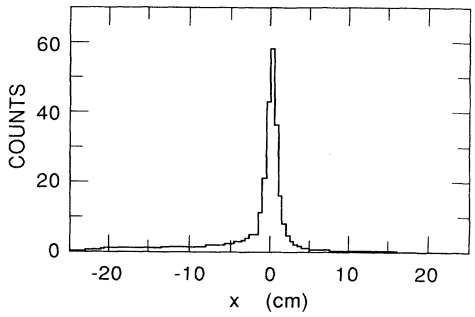

FIG. 14. The X-axis projection of the annihilation vertex, showing the preponderance of stopped annihilations over in-flight interactions.

In addition to the Q counter timing cut, several other event geometry and timing cuts were applied to the data to insure a clean data sample. Details regarding these cuts are reported in Refs. [7] and [8]

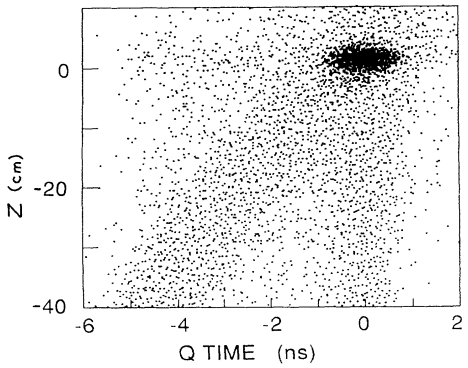

FIG. 15. The mean TDC spectrum for the Q-scintillation counter versus the vertex position along the target axis.

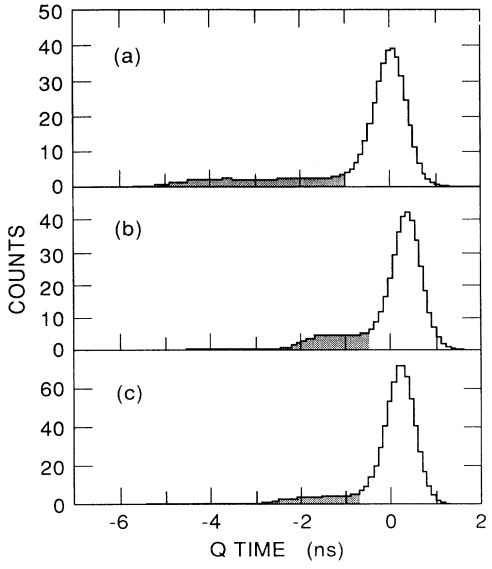

FIG. 16. The Q-counter timing cuts applied to the (a) 430 MeV/c $\bar{p} + H_2(l)$, (b) 350 MeV/c $\bar{p} + D_2(l)$, and (c) 350 MeV/c $\bar{p} + H_2(l)$ data sets. In-flight events are shaded.

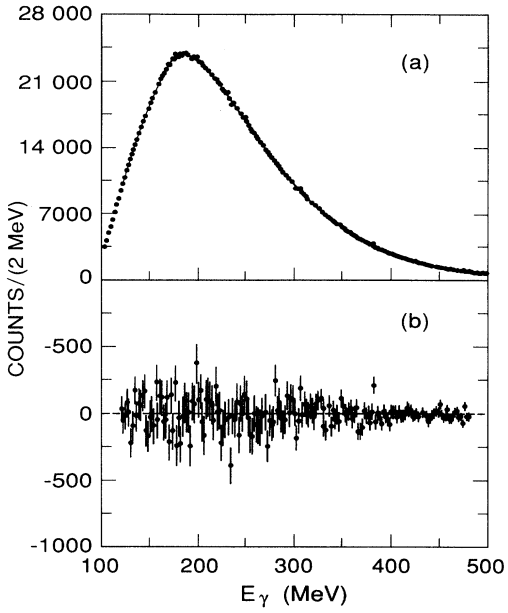

FIG. 18. Hydrogen 3.5-kG TT spectrum and fit.

VI. FINAL SPECTRA AND THE SEARCH FOR NARROW STATES

Figures 17–19 show the final γ-ray spectra resulting from the annihilation of antiprotons at rest in liquid hydrogen taken with a 3.5-kG field setting. Data taken at the higher field setting of 7.5 kG are presented in Figures 20–22. Figures 23–25 show the final γ-ray spectra resulting from the annihilation of antiprotons at rest in liquid deuterium. No clear evidence for narrow lines is seen in these spectra. Therefore, search procedures were developed that would allow one to conduct a search for narrow states and also to calculate the yield of any states

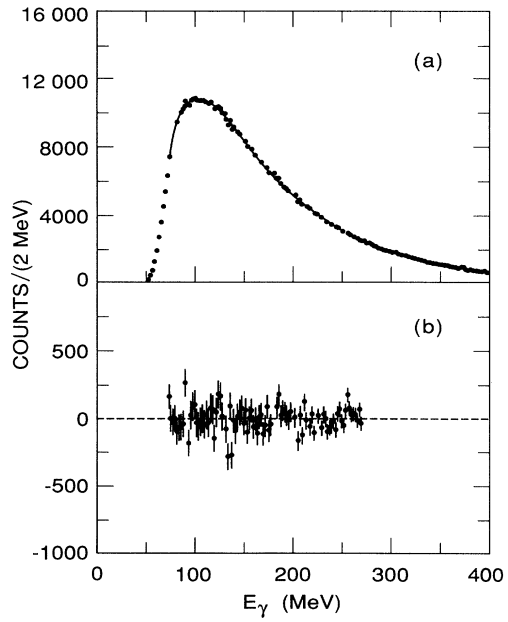

FIG. 17. Hydrogen 3.5-kG RT spectrum and fit.

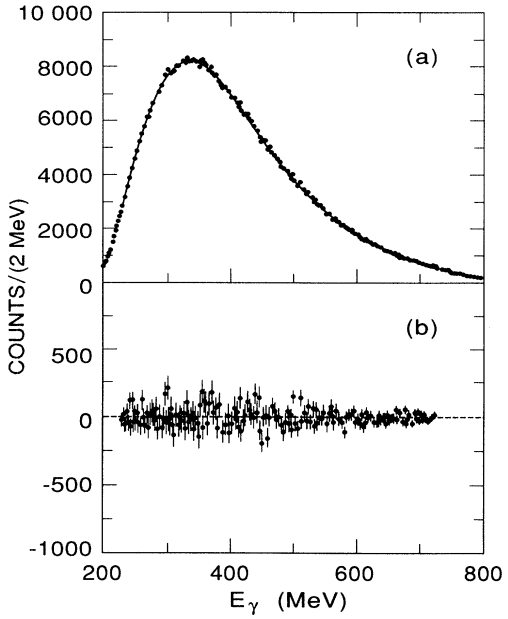

FIG. 19. Hydrogen 3.5-kG PT spectrum and fit.

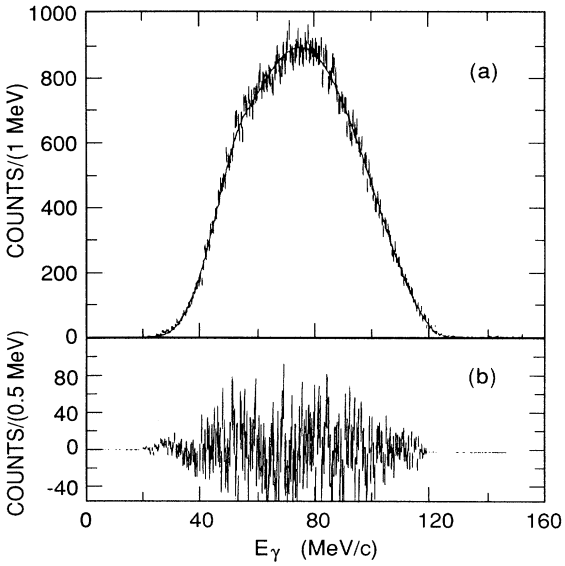

FIG. 20. Hydrogen 7.5-kG RR spectrum and fit.

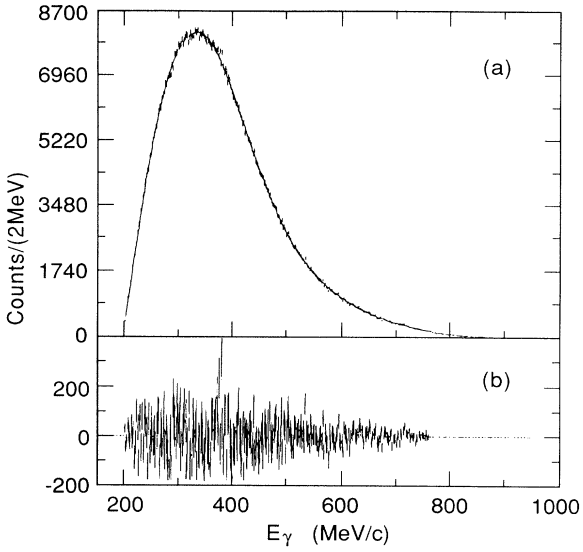

FIG. 22. Hydrogen 7.5-kG TT spectrum and fit.

found. In the absence of states, upper limits for the yield of narrow baryonium states were calculated.

A. The fitting routines

Although the Monte Carlo–generated spectra were qualitatively in good agreement with the data spectra, a Monte Carlo–background subtraction technique was not employed. Instead, the search was based on a global fit to the background spectrum of a low-order polynomial (to simulate the smooth π^0 induced background) plus a Gaussian function that simulated the response of the spectrometer to a monoenergetic γ ray. Low-order polynomials (fourth–eight order) were chosen to ensure that the fitted background was smooth and did not conform to all the statistical fluctuations (or peaks) inherent in the spectra. In order to fit the whole spectral region with a low-order polynomial, however, it was neccessary to divide the spectra into two regions: one below the

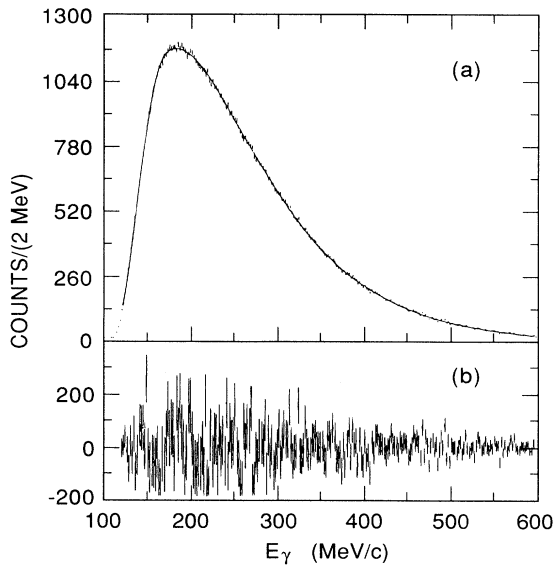

FIG. 21. Hydrogen 7.5-kG RT spectrum and fit.

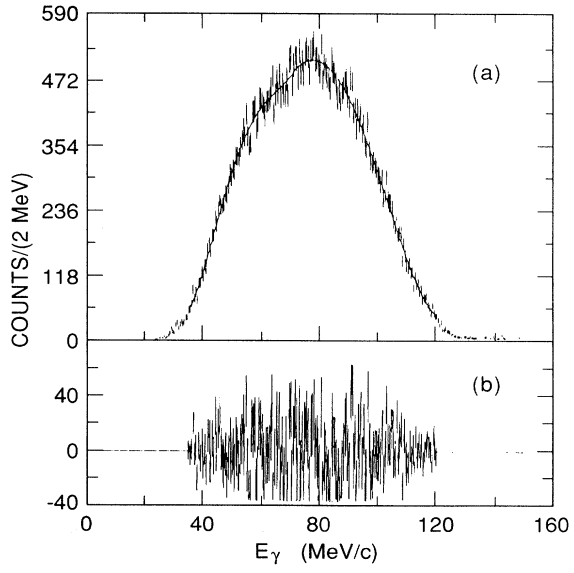

FIG. 23. Deuterium RR spectrum and fit.

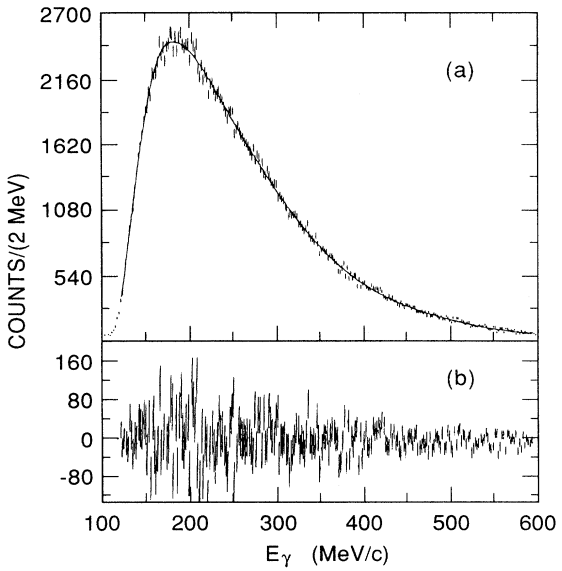

FIG. 24. Deuterium RT spectrum and fit.

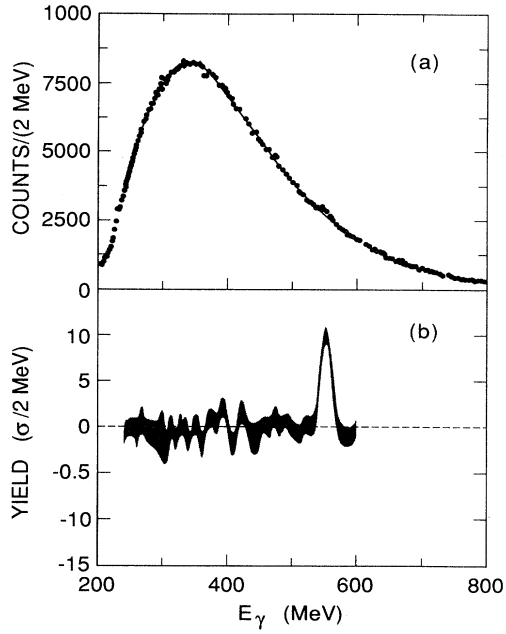

FIG. 26. Fake PT γ spectrum with a Gaussian peak inserted at the strength and location of a previously reported line. No structures of this significance exist in our spectra.

spectral maximum, the other above. Low-order polynomials were then independently fit to the two regions, with the constraint that they be continuous with continuous first derivative at their junction. The quality of the fits was quite high, with $\chi^2/N_{\rm DF}$ typically in the 0.98–1.3 range. The polynomial coefficients were then fixed, and the spectra were refit with the polynomial plus a Gaussian distribution. This fitting procedure was conducted on a bin-by-bin basis. The position of the Gaussian was constrained to the center of the bin and the width of the Gaussian (σ) was set by the resolution of the spectrometer for the momentum (of the bin) and topology type under consideration. Because of the Fermi motion of the nucleons in deuterium, there would be an intrinsic broadening of any monochromatic γ rays produced. This broadening was estimated using the Hulthen wave function and the Gaussian widths for the search of the deuterium data were correspondingly broadened by $\sim 4\%$. During the fit only the Gaussian peak height was allowed to vary. The fitting routine returned the peak height h along with its associated error Δh. The number of events in any peaks thus found is then simply related to the peak height by the formula $N = \sqrt{2\pi}\,\sigma h$, with an associated error of $\Delta N = \sqrt{2\pi}\,\sigma\,\Delta h$. This error in the signal can be attributed to both the statistical error resulting from the number of events in the peak and the errors resulting from the background under the signal region. Since the search was for narrow signals over large regions of background, the error is primarily due to the statistical error from the number of events in the peak. Indeed, the ratio of the error returned by the search routine to the statistical error in the number of events in the peak was found to be very close to one over the entire search region and for all the spectra. The smooth background is well approximated by the low-order polynomials as reflected by the small values of the χ^2 of the fit. In the absence of any real peaks in the data one would expect that the fitting routine should also find an equal amount of positive excess and negative deficit, due simply to the statistical nature of the variations in bin contents. The average residual, as well as the average of the absolute value, was in all cases found to be quite small. The yield of any peaks found (expressed in units of σ) was also found to be small, in accord with expectations.

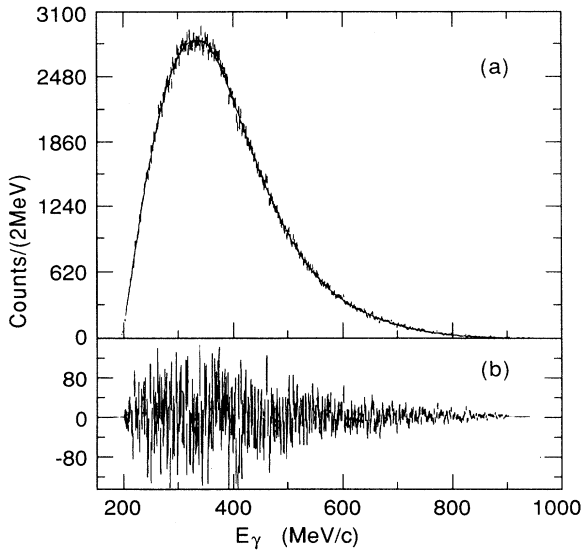

FIG. 25. Deuterium TT spectrum and fit.

B. Determining the yield

Normally, one relates the number of signal events, $N_{\rm signal}$, to the yield per $\bar{p}p$ annihilation via the relation:

$$Y_{\bar{p}p}(E_\gamma) = \frac{N_{\text{signal}}(E_\gamma)}{N_{\bar{p}p} A(E_\gamma)} ,$$

where $N_{\bar{p}p}$ is the total number of antiprotons for which the experiment was sensitive and $A(E_\gamma)$ is the acceptance of the spectrometer for an incident γ ray of energy E_γ. In addition to the geometrical acceptance of the spectrometer (well modeled by GEANT), triggering efficiencies for the separate event topologies and the number of antiprotons for which the spectrometer was live would have to be folded into the calculation. Comparing yield calculations in those regions where the spectra overlap would then be rather sensitive to errors in the determination of these factors. Therefore, a procedure which did not rely on an explicit expression for the spectrometer acceptance was utilized. The very good agreement of the Monte Carlo spectra with the data indicates that not only is the geometric acceptance of the spectrometer well understood, but the shape of the intrinsic background spectrum is also well described. This allows one to employ a procedure in which one relates the number of events in the fitted background (N_{bckgnd}) to the number of events in the intrinsic γ ray spectrum at each momentum bin. Since the intrinsic γ ray spectrum [$F(E_\gamma)$], has been normalized to one $\bar{p}p$ annihilation, the ratio is simply the number of antiprotons for which the system was live at that particular momentum. The yield is then simply

$$Y_{\bar{p}p}(E_\gamma) = N_{\text{signal}}(E_\gamma) \frac{F(E_\gamma)}{N_{\text{bckgnd}}} .$$

The statistical error in the yield is dominated by the statistical error associated with the signal. The branching ratios for the various exclusive channels of the $\bar{p}d$ annihilation are not as well known as those of $\bar{p}p$. Therefore, the intrinsic γ ray spectrum resulting from $\bar{p}d$ annihilations could not be modeled well. However, a comparison of the data spectra showed that the deuterium annihilation spectra are very similar to the hydrogen data spectra. The yield calculations for the deuterium data were therefore calculated assuming the same intrinsic spectral distribution as for the hydrogen data. The normalization of the spectrum was adjusted to reflect the average γ-ray multiplicity of 3.04 expected from annihilations in deuterium as opposed to 3.84 for hydrogen. From charge independence, the average number of charged pions produced in the deuterium annihilations is equal to twice the number of neutral pions produced. Therefore, the average γ-ray multiplicity is equal to the average charged multiplicity, which was taken from Ref. [18]. Several tests were carried out to ensure that the search procedure could not only detect narrow structures but also correctly calculate their yield. In one test, the size of the signal expected for the narrow line at $E_\gamma = 550$ MeV reported by a previous experiment (Richter *et al.* [5]) was checked. Based on the yield of the reported line (0.9×10^{-3}), a peak of ~ 1628 events is expected. When a peak of this magnitude is inserted into an artificial PT gamma spectrum, it stands out quite clearly as a 10σ effect, as seen in Fig. 26. The search procedure found the peak to contain 1820 ± 175 events.

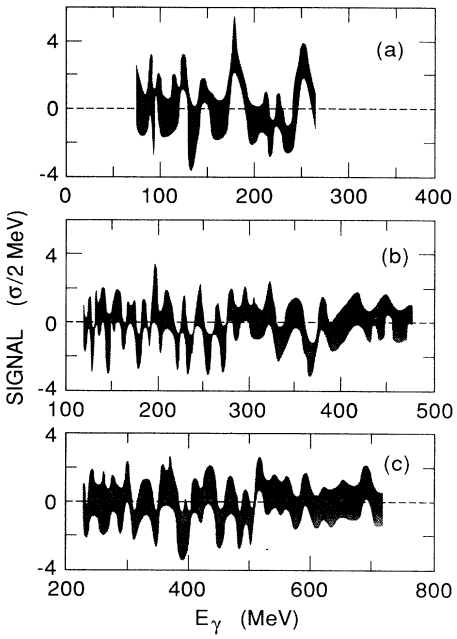

FIG. 27. Results of the hydrogen 3.5-kG spectrum search for RT, TT, and PT γ's, showing the statistical significance of structures found in the spectra.

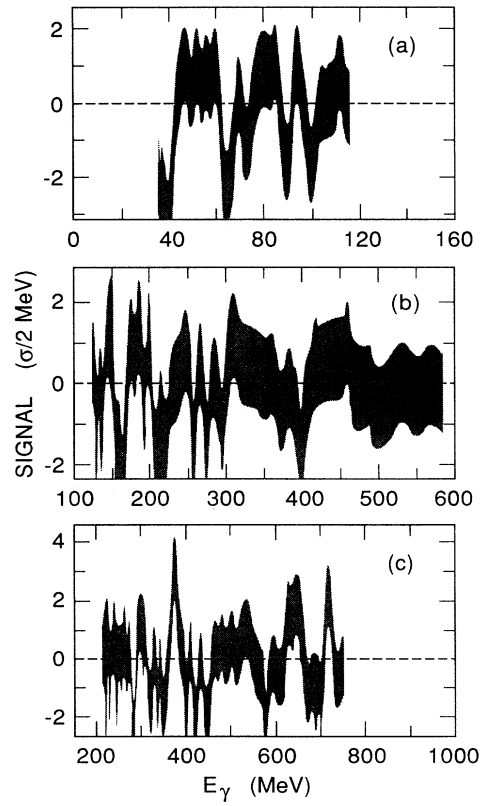

FIG. 28. Results of the hydrogen 7.5-kG spectrum search for RR, RT, and TT γ's, showing the statistical significance of structures found in the spectra.

C. Results of the search for narrow states

Once the efficacy of the search procedure had been demonstrated, the search for narrow structures in the spectra could be undertaken. Figures 27–29 show the results of the search of the data spectra. The plots show the statistical significance (in units of σ) of any structures found by the fitting program. The spectra are seen to be almost devoid of structure. The (1–2)σ fluctuations are consistent with that expected for data samples with purely statistical fluctuations. Also, in the region where the spectra overlap, any structure due to narrow states should be seen in both spectra, providing a consistency check. This allows one to rule out the apparent 3.7σ structure seen in the RT spectrum at $\sim$ 170 MeV/c, since no evidence is seen for it in the TT spectrum. Rather than quote yields for every one to three σ bump found by the search procedure, we instead calculate an upper limit on the yield of narrow lines found in the spectrum at the 95% confidence-level. The technique involves translating the significance of a particular peak (in units of sigma) into a corresponding 95% confidence level upper limit on the significance of the peak. For example, one can be 95% confident that a 1σ peak found in the experimental spectrum is in fact no larger than about 2.5σ. On the other hand, a 1σ dip found in the experimental spectrum can be assigned a 95% confidence upper limit of approximately 1.2σ. This assumes that the bumps and dips found in the spectra are statistical in nature, so that a statistical fluctuation below background serves to enhance sensitivity and thus gives a better yield limit. Details of the procedure for determining the yield limits can be found in Ref. [8]. Figure 30 shows the 95% confidence level upper limits on the yield of narrow structures in the γ-ray spectra resulting from the annihilation of antiprotons in liquid hydrogen at rest. The yields for the most prominent states reported by Richter *et al.* [5] are included for comparison. These yield limits were obtained from the 3.5-kG data, no attempt being made to combine the limits from those obtained at the higher field setting. In Fig. 31 are shown the corresponding 95% confidence

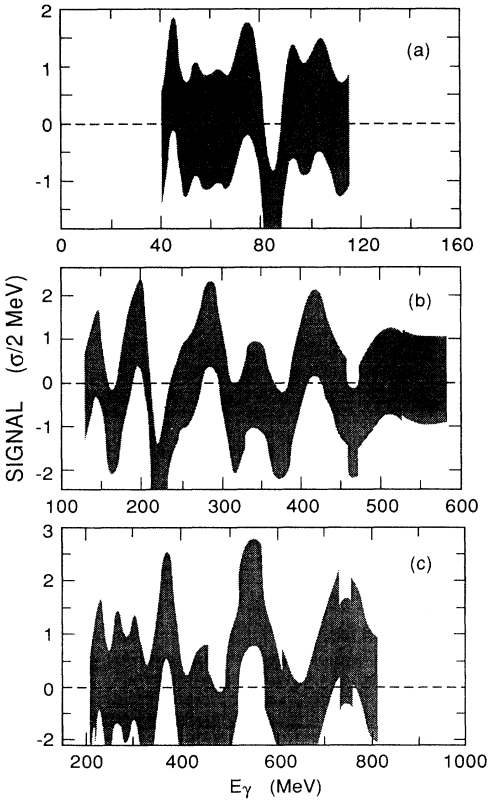

FIG. 29. Results of the deuterium spectrum search for RR, RT, and TT γ's, showing the statistical significance of structures found in the spectra.

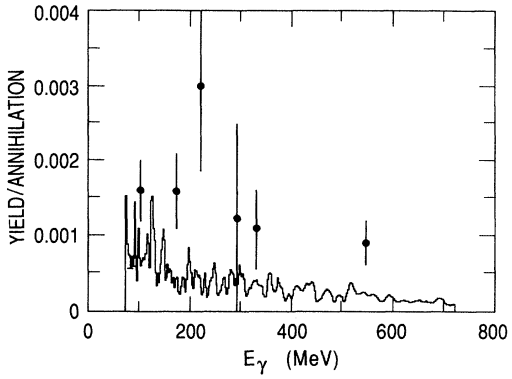

FIG. 30. Shown are the 95% confidence level upper limits on the yield for the reaction $\bar{p}p \rightarrow \gamma X$, for states narrower than the spectrometer resolution (3.5-kG field setting). Also shown are the most prominent lines reported in Ref. [15].

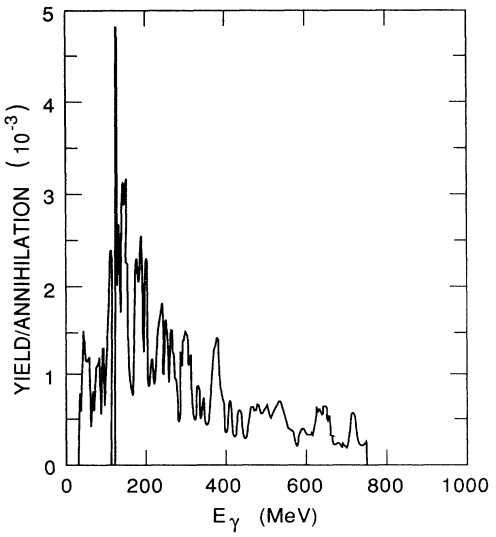

FIG. 31. Shown are the 95% confidence level upper limits on the yield for the reaction $\bar{p}p \rightarrow \gamma X$, for states narrower than the spectrometer resolution (7.5-kG field setting).

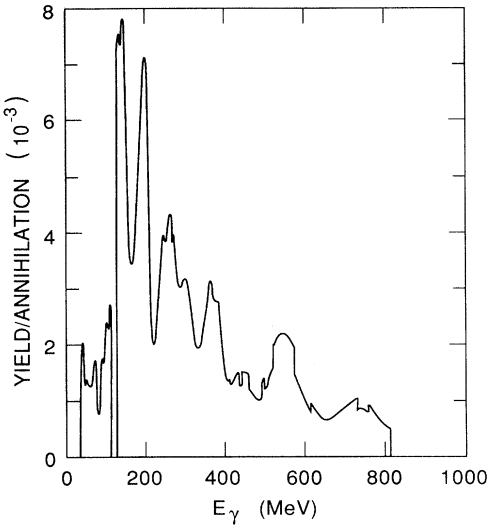

FIG. 32. Shown are the 95% confidence level upper limits on the yield for the reaction $\bar{p}d \rightarrow \gamma X$, for states narrower than the spectrometer resolution.

level upper limits on the yield of narrow structures in the data accumulated at 7.5 kG. The relatively poorer limits are simply due to the smaller number of events in the second-run data sample. Figure 32 shows the corresponding limits in the γ-ray spectra resulting from the annihilation of antiprotons in liquid deuterium at rest.

D. Conclusions

A detailed search of the γ spectra resulting from antiproton annihilations at rest in liquid hydrogen and deuterium has yielded no convincing evidence of radiative transitions to narrow states with widths consistent with the spectrometer resolution ($\delta E/E \simeq 1\%$). In liquid hydrogen, we obtain upper limits at the 95% confidence level on the yield of narrow states produced in proton-antiproton annihilations at rest of $(2\text{–}5)\times 10^{-4}/\bar{p}$ for states between 1000 and 1700 MeV, and $(5\text{–}10)\times 10^{-4}/\bar{p}$ for states between 1700 and 1800 MeV. For annihilations in liquid deuterium the upper limits are $(1\text{–}7)\times 10^{-3}/\bar{p}$ for masses between 400 and 1730 MeV/c^2, and $(1\text{–}2)\times 10^{-3}/\bar{p}$ for masses between 1750 and 1835 MeV/c^2.

In addition to our experiment, two other recent exper-

TABLE II. Comparision of the current limits on narrow lines resulting from antiproton annihilations at rest. Included are the previously published results on the existence of such lines.

Experiment	Ref.	Reaction	Mass (MeV)	Yield (10^{-3})	Confidence (σ or % C.L.)
Gray *et al.*	[24]	$\bar{p}d \rightarrow pX_{\bar{p}n}$	1794.5 ± 1.4	4 ± 0.6	~ 5
Pavlopoulos *et al.*	[5]	$\bar{p}p \rightarrow \gamma X$	1684 ± 8	7 ± 2	2.6
			1646 ± 9	6 ± 2	2.2
			1394 ± 23	9 ± 2	2.4
Richter *et al.*	[5]	$\bar{p}p \rightarrow \gamma X$	1771 ± 1	1.6 ± 0.4	3.6
			1691 ± 2	1.6 ± 0.5	3.1
			1642 ± 6	3.0 ± 1.1	2.7
			1555 ± 3	1.2 ± 0.5	2.7
			1504 ± 4	1.1 ± 0.5	2.2
			1208 ± 4	0.9 ± 0.5	3.0
Adiels *et al.*	[5]	$\bar{p}^4He \rightarrow \gamma X 3n$	1687 ± 5	9.3 ± 1.8	5.5
			1640 ± 12	8.9 ± 1.9	5.2
Brando *et al.*	[5]	$\bar{p}p \rightarrow \gamma X$	1768 ± 3	10 ± 3	3.3
Ahmad *et al.*	[25]	$\bar{p}p \rightarrow \pi^{\pm}X^{\mp}$	1100 – 1670	< 2.0	5
Angelopoulos *et al.*	[11]	$\bar{p}p \rightarrow \pi^{\pm}X^{\mp}$	1510 – 1660	$< 0.2 - 0.6$	90%
	[23]	$\bar{p}p \rightarrow \pi^{\pm}X^{\mp}$	350 – 1516	$< 0.3 - 0.6$	90%
	[23]	$\bar{p}p \rightarrow K^{\pm}X^{\mp}$	629 – 1175	< 0.15	90%
	[6, 8]	$\bar{p}p \rightarrow \gamma X$	1000 – 1700	$< 0.2 - 0.5$	95%
	[6, 8]	$\bar{p}p \rightarrow \gamma X$	1700 – 1800	$< 0.5 - 1.0$	95%
Chiba *et al.*	[21]	$\bar{p}p \rightarrow \gamma X$	1086 – 1787	$< 0.1 - 0.5$	90%
Adiels *et al.*	[22]	$\bar{p}p \rightarrow \gamma X$	1040 – 1770	$< 0.1 - 0.3$	95%

iments have also examined the inclusive γ spectrum from $\bar{p}p$ annihilations at rest. The first of these was experiment E68 performed at KEK using a traditional secondary beam [21]. Antiprotons of 580 MeV momentum were stopped in a large (14×23 cm) liquid-hydrogen target after moderation in a graphite degrader. The γ rays were detected using a large 96 crystal NaI(Tl) spectrometer with good solid angle coverage (22% of 4π). Their energy resolution is quoted as $\Delta E_\gamma/E_\gamma = 6.2\%/[E_\gamma\ (\mathrm{GeV})]^{1/4}$ FWHM. Aside from a prominent Panofsky γ signal, they noticed no structure greater than 2σ in significance in the energy range $87 < E_\gamma < 624$ MeV, corresponding to recoil masses between 1086 and 1787 MeV. They place a 4σ upper limit on the existence of narrow structures of between 1.2×10^{-3} and 6×10^{-4}.

The second experiment, PS182 at LEAR, was performed during the same period as our experiment [22]. Here 320 MeV/c antiprotons were stopped in a liquid-hydrogen target of 20 cm length and 5 cm diameter. They measured the γ rays produced in the annihilation with a set of 2 BGO crystal arrays consisting of 7 hexagonal prisms each and covering an effective solid angle of about 0.1% of 4π. Their energy resolution is stated as $\Delta E_\gamma/E_\gamma = 4.0\%/[E_\gamma\ (\mathrm{GeV})]^{1/4}$ FWHM. They place a limit on the yield of narrow structures of between 10^{-3} and 10^{-4} for states with masses between 1040 and 1770 MeV/c^2.

In comparison with the crystal arrays used in these other experiments, the magnetic spectrometer used in our experiment has better resolution throughout the energy spectrum. On the other hand the crystal spectrometers have the advantage of flat geometrical acceptance functions, enabling them to see clearly the shape of the inclusive γ spectrum. They are also able to see a clear Panofsky signal in their uncut inclusive γ spectrum. Our Panofsky line appears in relatively low acceptance regions of the 3.5-kG RT and TT γ spectra and can only be extracted with a Q counter timing cut. Nevertheless, the superior energy resolution enables us to set a good limit on the existence of narrow lines over a fairly large mass region.

The results of this experiment, along with the results of the two independent experiments discussed above, clearly contradict earlier results claiming the existence of γ transitions to narrow quasinuclear or baryonium states below threshold.

It should also be noted that, using the magnetic spectrometer as a charged particle spectrometer, we have also set limits on the production of narrow states via the emission of a charged pion or kaon. Upper limits of $(2\text{–}6)\times 10^{-4}/\bar{p}$ were set on the yield of a narow state in the case of pion emission [11]. In the case of emission of a charged kaon, upper limits of $(3\text{–}6)\times 10^{-4}$ were set in the mass range between 350 and 1516 MeV [23]. The results of the various searches are shown in Table II, as well as the results from the previous experiments.

ACKNOWLEDGMENTS

This work was supported in part by the Greek Ministry of Research and Technology, U.S. National Science Foundation, U.S. Department of Energy, and the Federal Ministry for Research and Technology, FRG.

* Present address: Fermi National Laboratory, Batavia, IL 60510.
† Present address: Stanford Linear Accelerator, Stanford, CA 94305.
‡ Present address: Paul Scherrer Institute, Villigen, Switzerland, CH-5232.

[1] I.S. Shapiro, Phys. Rep. **35**, 129 (1978).
[2] G.C. Rossi and G. Veneziano, Phys. Rep. **63**, 153 (1980).
[3] C.B. Dover, J.M. Richard, and M.C. Zabek, Ann. Phys. (N.Y.) **130**, 70 (1980).
[4] R.L. Jaffe and K. Johnson, Phys. Lett. **60B**, 201 (1976); R.L. Jaffe, Phys. Rev. D **15**, 267 (1977); **15**, 281 (1977); **17**, 1444 (1978).
[5] P. Pavlopoulos *et al.*, Phys. Lett. **72B**, 415 (1978); B. Richter *et al.*, *ibid.* **126B**, 284 (1983); T. Brando *et al.*, *ibid.* **139B**, 133 (1984); L. Adiels *et al.*, *ibid.* **138B**, 235 (1984).
[6] A. Angelopoulos *et al.*, Phys. Lett. B **178**, 441 (1986).
[7] N. A. Graf, Ph.D. dissertation, Univ. of Calif., Irvine, 1989.
[8] M. J. Fero, Ph.D. dissertation, Univ. of Calif., Irvine, 1988.
[9] L. Bürcker, Diplomarbeit, Universität Karlsruhe, 1989 (KfK Report No. 4509).
[10] J. Schwertel, Diplomarbeit, Universität Karlsruhe, 1987 (KfK Report No. 4359).
[11] A. Angelopoulos *et al.*, Phys. Lett. **159B**, 210 (1985).
[12] C.A. Benulis and W.K. McFarlane, Nucl. Instrum. Methods **A240**, 130 (1985).
[13] G. Büche and H. Koch, KfK report (unpublished).
[14] W. Chinowsky and G. Kojoian, Nuovo Cimento A **3**, 684 (1966).
[15] G. Backenstoss *et al.*, Phys. Lett. B **228**, 424 (1983).
[16] T.E. Kalogeropoulos *et al.*, Phys. Rev. D **26**, 543 (1982).
[17] G. Ghesquière, in *Proceedings of the Symposium on Antinucleon-Nucleon Interactions*, Liblice-Prague, Czechoslovakia, 1974, edited by L. Montanet (CERN Report No. 74-18, Geneva, Switzerland, 1974), p. 436.
[18] T. Kalogeropoulos *et al.*, Phys. Rev. Lett. **33**, 1631 (1974); **33**, 1635 (1974).
[19] C. Amsler *et al.*, Phys. Rev. Lett. **44**, 853 (1980).
[20] T. Usher, Ph.D. dissertation, Univ. of Calif., Irvine, 1989.
[21] M. Chiba *et al.*, Phys. Rev. D **36**, 3321 (1987).
[22] L. Adiels *et al.*, Phys. Lett. B **182**, 405 (1986).
[23] M. Soulliere, Ph.D. dissertation, Penn. State Univ., 1987.
[24] L. Gray, P. Hagerty, and T. Kalogeropoulos, Phys. Rev. Lett. **26**, 1491 (1971).
[25] S. Ahmad *et al.*, Phys. Lett. **157B**, 333 (1986).